Coordination of Converter and Fuel Cell Controllers

Kyung-Won Suh and Anna G. Stefanopoulou

Department of Mechanical Engineering, University of Michigan, Ann Arbor, MI 48109, U.S.A

Abstract

Load following fuel cell systems depend on control of reactant flow and regulation of DC bus voltage during load (current) drawn from them. To this end, we model and analyze the dynamics of a fuel cell system equipped with a compressor and a DC-DC converter. We then employ model-based control techniques to tune two separate controllers for the compressor and the converter. We demonstrate that the lack of communication and coordination between the two controllers entails a severe tradeoff in achieving the stack and power output objectives. A coordinated controller is finally designed that manages the air and the electron flow control in an optimal way. We demonstrate our results during specific and critical load changes around a nominal operating point. Although our analysis does not cover wide operating region, it provides insight on the level of controller coordination necessary in non-hybridized fuel cell power supply. The shut-down and start-up procedures will be investigated in future work.

Keywords: Fuel cells, Converters, Compressors, Control

1 Introduction

Portable, stationary and automotive propulsion power applications impose stringent requirements on the transient behavior of proton exchange membrane (PEM) fuel cells (FC). Transient response is a key characteristic feature of backup power system, sometimes more critical than efficiency, due to the importance of accepting uncertain electric loads. Fast transient response is also essential for autonomy in startup and fast power response for automotive fuel cells. For these reasons, every fuel cell power system is expected to produce power on demand, also known as, a load following fuel cell. Fuel cells, however, are typically known to be slower than any other power sources due to the complex dynamics associated with mass and heat balances inside and outside the stack. To address these limitations, a PEM fuel cell system is typically combined with a battery or capacitor into a hybrid power generation system.

A complete PEM fuel cell power system includes several components apart from the fuel cell stack and battery, such as an air delivery system which supplies oxygen using a compressor or a blower, a hydrogen delivery system using pressurized gas storage or reformer, a thermal and water management system that handles temperature and humidity, DC-DC converters to condition the output voltage and/or current of the stack and finally electric loads [19, 25]. Figure 1 shows the configuration of a typical fuel cell power system which is constructed with fuel cell, DC-DC converter and battery.

The DC-DC converter transforms unregulated DC power of the FC to regulated DC bus power. Research on the DC-DC converters for fuel cells is focused on soft voltage sources which
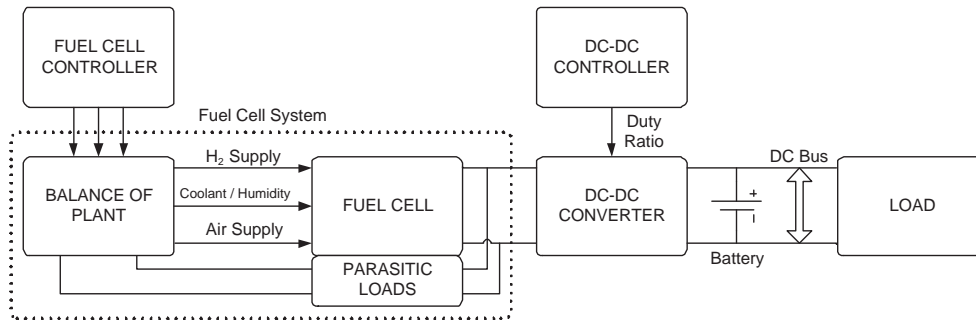
Figure 1: Block diagram of a typical fuel cell power system

accounts for the cell voltage variation due to the electrochemical characteristic at different operation conditions [15]. Sometimes the converter is used to filter the current from the fuel cells to avoid imposing transients that can lead to FC failure or degradation. In both cases, the coupled dynamics of current and voltage in fuel cells and the converter affects the system performance. Specifically, limiting the current drawn from the fuel cell enhances fuel cell performance but degrades the voltage regulation performance in DC-DC converter. This direct conflict can be addressed easily with hybridization.

Hybridization in the fuel cell power system may also achieve higher fuel cell efficiency by leveling peak power demand to the battery, allowing the fuel cell to operate on its optimum range. Cunningham *et al.* [3] showed that battery-hybrid fuel cell vehicle associated with regenerative braking improves efficiency up to 15 %. The efficiency gain in a fuel cell hybrid vehicle depends on the degree of hybridization [12]. The hybrid system efficiency can be even worse than the stand-alone fuel cell in some driving cycles [8, 20]. Also, efficiency of a hybridized auxiliary power unit (APU) or distributed power generation, which has no energy recovery apparatus like regenerative braking, is not yet addressed. These unexplored issues highlight the importance of defining the achievable performance and limitation of a fuel cell power system before hybridization.

The purpose of this paper is to define the dynamic limitation of a FC power system which is augmented with a DC-DC converter but without a battery. To investigate the coupled dynamics with currents and voltages in the fuel cell power system, it is necessary to establish an analytic model for the fuel cell with DC-DC converter and design the overall system.

We first develop a physics-based model for reactant supply dynamics of the fuel cell stack and the power electronics of the DC-DC converter. The fuel cell stack and reactant flow models are based on electrochemistry, mass balances for lumped volumes in the stack and peripheral volumes, and rotational dynamics of compressor and motor. We neglect hydrogen dynamics assuming pressurized hydrogen storage is available. We also neglect humidity and temperature dynamics because they are slower than the air flow dynamics [1, 24]. The significance of the air supply arises due to its considerable parasitic losses [5]. In this paper, we introduce another important aspect of air flow control, namely, the dynamic coupling between the compressor and the fuel cell when the compressor motor is driven by the stack power.

The dynamic behavior of voltages and currents between the input source and the output load of the DC-DC converter is explained by a simple transient model. The actual converter operates by switching pulse devices, but it is approximated by an average model that captures transient dynamics within the bandwidth of the switching frequency.

In the controller design stage, the fuel cell reactants' supply and DC-DC converter are treated separately. In other words, the controller is first designed for the best performance of each plant in a decentralized fashion. Then, each controller is re-tuned sequentially in favor of the

other because there is a direct conflict between performance objectives of the fuel cells and the converter. We then introduce coordination in a combined system controller with optimal gains. The coordinated control accounts for the interactions between the two systems and allows us to construct a controller for the best possible performance. The results of the dynamic model analysis and control study in this paper provides the insight on the fundamental system controllability and limitations in handling transient load in a fuel cell power system.

2   Fuel cell system with air flow control

We consider a fuel cell stack with active cell area of $A_{fc} = 280$ cm^2 and $n = 381$ number of cells with 75 kW gross power output that is applicable to the automotive and residential areas. The performance variables for the FC power system are (i) the stack voltage v_{st} that directly influences the stack power generated $P_{fc} = v_{st}I_{st}$ when the load (current) I_{st} is drawn from the stack, and (ii) the oxygen excess ratio λ_{O_2} in the cathode that indirectly ensures adequate oxygen supply to the stack.

Stack voltage is calculated as the product of the number of cells and cell voltage $v_{st} = nv_{fc}$. The combined effect of thermodynamics, kinetics, and ohmic resistance determines the output voltage of the cell, as defined by

$$v_{fc} = E - v_{act} - v_{ohm} - v_{conc} \tag{1}$$

where E is the open circuit voltage, v_{act} is the activation loss, v_{ohm} is the ohmic loss, and v_{conc} is the concentration loss. The detailed formulation of the FC voltage, also known as, polarization characteristic can be found in [16].

In steady state, FC voltage is given as static function of current density $i_{fc} = I_{st}/A_{fc}$ and several other variables such as oxygen and hydrogen partial pressures p_{O_2} and p_{H_2}, cathode pressure p_{ca}, temperature T_{st} and humidity λ_m. Although we assume instantaneous electrochemical reaction and negligible electrode double layer capacity, the FC voltage has a rich dynamic behavior due to its dependance on dynamically varying stack variables $(i_{fc}, p_{O_2}, p_{ca}, p_{H_2}, T_{st}, \lambda_m)$. In this paper, we assume compressed hydrogen supply as shown in Figure 2, which simplifies the control of anode reactant flow. We also assume that the stack temperature and humidity is controlled accurately and with negligible lag. Perfect cooler and humidifier are assumed for this work.

In this paper, we concentrate on the dynamic behavior of the variables associated with the air flow control, namely, oxygen pressure p_{O_2}, total cathode pressure p_{ca}, and oxygen excess ratio in the cathode λ_{O_2}, which is a lumped parameter that indicates the amount of oxygen supplied versus oxygen consumed. All variables associated with the air supply and the stack performances are defined in the following sections. The transient voltage changes in the stack are minimized using precise control of reactants. However, the flow dynamics of the oxygen and hydrogen reactants are governed by pressure dynamics through flow channels, manifolds, orifices. Also, fuel cells are required to have an excessive amount of oxygen and hydrogen flow into the stack to avoid stagnant vapor and nitrogen films covering the electrochemical area.

Depending on the load (current) drawn from the fuel cell and the air supply to the fuel cell, the stack voltage varies between 200 V to 300 V. The air is supplied by a compressor that is driven by a motor with maximum power of 15 kW. At its maximum rotational speed of 100 kRPM the compressor provides 95 g/sec of air flow and generates a pressure increase of 3.5 atm. The maximum compressor air flow is twice the air flow necessary to replenish the oxygen consumed from the stack when the maximum current is drawn $I_{st,max} = 320$ A. The maximum FC current is defined as the current at which the maximum FC power is achieved. Drawing more current from the fuel cell results in rapid decrease of the stack voltage, and thus power due to concentration losses [14].
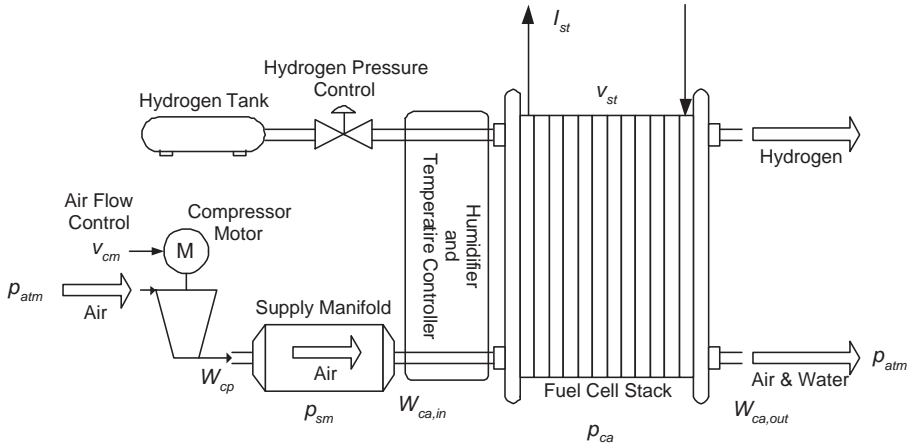
Figure 2: Fuel cell reactant supply system

Although the compressor absorbs a significant amount of power and increases the fuel cell parasitic losses, it is preferred to a blower due to the resulting high power density (kW/m^3). A blower is typically not capable of pushing high flow rates through small channels. The blower requires large channel volumes, and thus larger stacks. Note here that there have been many studies analyzing the tradeoff between FC power density and parasitic losses from the air supply device [4]. Additional considerations associated with controlling the system humidity and temperature depending on the operational pressure are still under debate [9]. Comparison of the dynamic flow capabilities of a FC system with a blower and a compressor can be found in [10]. It is shown that the two systems are dynamically similar in providing air flow in the cathode channels. The blower spends time spinning its rotor inertia, whereas the compressor spends time pushing the air and elevating the supply manifold pressure.

The tradeoff between satisfying net power requirements and maintaining optimum oxygen excess ratio in the stack during load step changes is first defined in [16]. We show here that this tradeoff is more critical when the compressor motor draws its power directly from the fuel cell instead of an auxiliary power source. The limitations are analyzed in Section 2.3 after developing a low order fuel cell model in Section 2.1 and 2.2. A proportional integral (PI) controller is developed in Section 2.3. For the air flow controller we assume fast changes in the load (current) drawn from the fuel cell. In Section 3 we investigate how DC-DC converter can be used to filter fast load changes.

2.1 Dynamic states

Details of the model used in this study can be found in [16, 18]. Several simplifications and modifications have been employed to allow us to concentrate on the fast dynamics associated with the integration of a fuel cell with a converter. Specifically, the following assumptions are made: (i) All gases obey the ideal gas law; (ii) The temperature of the air inside the cathode is equal to the bulk stack temperature which is, in turn, equal to the temperature of the coolant exiting the stack; (iii) The properties of the flow exiting the cathode such as temperature and pressure are assumed to be the same as those inside the cathode and are the ones that dominate the reaction at the catalyst layers in the membrane; (iv) The gases in the anode and cathode are fully humidified and the water inside the cathode is only in vapor phase assuming any extra water turns to liquid and is removed from the channels; (v) We neglect flooding of the gas diffusion

4

layer; (vi) Finally, the flow channel and the gas diffusion layer are lumped into one volume, i.e., the spatial variations are neglected. Note here that all these assumptions are made to isolate the potential problems associated with non-hybridized load-following fuel cell that supports its external and auxiliary loads through its bus. By assuming perfect humidity and temperature regulation, we do not wish to underestimate their importance nor the challenges associated with the specific control task. We present the model dynamic states first and then in Section 2.2, we describe the nonlinear relationships that connect the inputs with the states and the outputs (performance variables and measurements for control).

The mass continuity of the oxygen and nitrogen inside the cathode volume and ideal gas law yield

$$\frac{dp_{O_2}}{dt} = \frac{\bar{R}T_{st}}{M_{O_2}V_{ca}} \left(W_{O_2,in} - W_{O_2,out} - W_{O_2,rct} \right), \tag{2}$$

$$\frac{dp_{N_2}}{dt} = \frac{\bar{R}T_{st}}{M_{N_2}V_{ca}} \left(W_{N_2,in} - W_{N_2,out} \right) \tag{3}$$

where V_{ca} is the lumped volume of cathode, $\bar{R}$ is the universal gas constant, and M_{O_2} and M_{N_2} are the molar mass of oxygen and nitrogen, respectively.

The compressor motor state is associated with the rotational dynamics of the motor through thermodynamic equations. A lumped rotational inertia is used to describe the compressor with the compressor rotational speed ω_{cp}

$$\frac{d\omega_{cp}}{dt} = \frac{1}{J_{cp}} \left(\tau_{cm} - \tau_{cp} \right) \tag{4}$$

where τ_{cm} is the compressor motor torque and τ_{cp} is the load torque of the compressor.

The rate of change of air pressure in the supply manifold that connects the compressor with the fuel cell (shown in Figure 2) depends on the compressor flow into the supply manifold W_{cp}, the flow out of the supply manifold into the cathode $W_{ca,in}$ and the compressor flow temperature T_{cp}.

$$\frac{dp_{sm}}{dt} = \frac{\bar{R}T_{cp}}{M_{a,atm}V_{sm}} \left(W_{cp} - W_{ca,in} \right) \tag{5}$$

where V_{sm} is the supply manifold volume and $M_{a,atm}$ is the molar mass of atmospheric air.

2.2   Nonlinear static functions

The nonlinear relations that connect the dynamics states (pressure and rotational speed) through the right-hand side of equations (2) - (5) are described in this section.

The inlet mass flow rate of oxygen $W_{O_2,in}$ and nitrogen $W_{N_2,in}$ can be calculated from the inlet cathode flow $W_{ca,in}$ as follows

$$W_{O_2,in} = \frac{x_{O_2,atm}}{1 + w_{atm}} W_{ca,in}, \tag{6}$$

$$W_{N_2,in} = \frac{1 - x_{O_2,atm}}{1 + w_{atm}} W_{ca,in} \tag{7}$$

where $x_{O_2,atm}$ is the oxygen mass fraction of the inlet air

$$x_{O_2,atm} = \frac{y_{O_2,atm}M_{O_2}}{y_{O_2,atm}M_{O_2} + (1 - y_{O_2,atm})M_{N_2}} \tag{8}$$

with the oxygen molar ratio $y_{O_2,atm} = 0.21$ and the humidity ratio of inlet air

$$w_{atm} = \frac{M_v}{y_{O_2,atm}M_{O_2} + (1 - y_{O_2,atm})M_{N_2}} \frac{\phi_{atm}p_{sat}}{p_{atm} - \phi_{atm}p_{sat}} \tag{9}$$

where $p_{sat} = p_{sat}(T_{st})$ is vapor saturation pressure and ϕ_{atm} is the relative humidity at ambient conditions which is preset to the average value of 0.5.

The supply manifold model describes the mass flow rate from the compressor to the outlet mass flow. A linear flow-pressure condition is assumed for the flow calculation due to the small pressure difference between the supply manifold and the cathode

$$W_{ca,in} = k_{ca,in}(p_{sm} - p_{ca}) \tag{10}$$

where $k_{ca,in}$ is the supply manifold orifice flow constant and spatially invariant cathode pressure p_{ca} is the sum of oxygen, nitrogen and vapor partial pressures

$$p_{ca} = p_{O_2} + p_{N_2} + p_{sat}. \tag{11}$$

The total flow rate at the cathode exit $W_{ca,out}$ is calculated by the nozzle flow equation [23] because the pressure difference between the cathode and the ambient pressure is large in pressurized stacks.

The rate of oxygen consumption $W_{O_2,rct}$ in (2) from the stack current I_{st} is given by

$$W_{O_2,rct} = M_{O_2}\frac{nI_{st}}{4F} \tag{12}$$

where n is the number of cells in the stack and F is the Faraday number.

The oxygen excess ratio λ_{O_2} that indicates oxygen starvation is defined as

$$\lambda_{O_2} = \frac{W_{O_2,in}}{W_{O_2,rct}}. \tag{13}$$

We assume vapor is saturated in the anode without flooding or nitrogen diffusion. We also assume that the anode pressure is regulated to follow the cathode pressure. Based on these assumptions, the hydrogen pressure that affects the FC voltage is calculated;

$$p_{an} = p_{ca}, \tag{14}$$
$$p_{H_2} = p_{an} - p_{sat}. \tag{15}$$

The outlet mass flow rate of oxygen $W_{O_2,out}$ and nitrogen $W_{N_2,out}$ used in (2) and (3) are calculated from the mass fraction of oxygen and nitrogen in the stack after the reaction

$$W_{O_2,out} = \frac{M_{O_2}p_{O_2}}{M_{O_2}p_{O_2} + M_{N_2}p_{N_2} + M_vp_{sat}}W_{ca,out}, \tag{16}$$

$$W_{N_2,out} = \frac{M_{N_2}p_{N_2}}{M_{O_2}p_{O_2} + M_{N_2}p_{N_2} + M_vp_{sat}}W_{ca,out}. \tag{17}$$

The compressor motor torque τ_{cm} is calculated assuming a simplified DC motor model with a static electromechanical relation of applied motor input voltage v_{cm} and back emf:

$$\tau_{cm} = \eta_{cm}\frac{k_t}{R_{cm}}(v_{cm} - k_v\omega_{cp}) \tag{18}$$

where k_t, k_v, and R_{cm} are motor constants and η_{cm} is the motor mechanical efficiency. The assumption of a voltage-controlled DC motor instead of frequency/amplitude controlled AC motor implies instantaneous generation of motor torque (v_{cm} to τ_{cm} relationship), neglecting all the high frequency dynamics associated with more realistic and modern switching drive. Our assumption can be justified because the switching frequency of the drive and the motor flux dynamics are faster than the dynamics of the combined motor-compressor inertia in equation (4). Even the implementation of a filter that minimizes the switching ripples preserves the highly dynamic (almost instantaneous) relationship between the motor control command (v_{cm} in our case) and the torque generation τ_{cm}. One will need to convert the voltage control command v_{cm} derived later in equation (24) and (31) to current or frequency/amplitude control command when specific motor and drive design are specified. The torque consumed by the compressor is calculated from the thermodynamic equation

$$\tau_{cp} = \frac{C_p}{\omega_{cp}} \frac{T_{atm}}{\eta_{cp}} \left[\left(\frac{p_{sm}}{p_{atm}} \right)^{\frac{\gamma-1}{\gamma}} - 1 \right] W_{cp} \tag{19}$$

where C_p and γ correspond to the constant-pressure and the ratio of the specific heat capacities of the air.

The compressor motor power P_{cm} provided by the compressor motor is calculated using the compressor motor voltage input v_{cm} and its rotational speed ω_{cp}

$$P_{cm} = \frac{v_{cm}}{R_{cm}} (v_{cm} - k_v \omega_{cp}). \tag{20}$$

This power can be supplied directly from the fuel cell or from an auxiliary power source.

The compressor flow W_{cp} is modeled by applying the Jensen and Kristensen nonlinear fitting method [16] as functions of the pressure ratio p_{sm}/p_{atm}, the upstream temperature T_{atm}, and the compressor rotational speed ω_{cp}. The temperature of the air leaving the compressor is modeled based on [16] with a map of the compressor efficiency η_{cp}

$$T_{cp} = T_{atm} + \frac{T_{atm}}{\eta_{cp}} \left[\left(\frac{p_{sm}}{p_{atm}} \right)^{\frac{\gamma-1}{\gamma}} - 1 \right]. \tag{21}$$

To demonstrate the FC model characteristics, a series of step changes in stack load (current) and compressor motor input voltage are applied to the stack and important FC variables are plotted in Figure 3. During the first three steps, the compressor voltage is controlled so that the oxygen excess ratio at 2 is maintained using a simple static feedforward controller. The remaining steps are then applied independently, resulting in different levels of oxygen excess ratios.

During a positive load step, the oxygen excess ratio drops due to the depletion of oxygen, that correlates well with the drop in the stack voltage. The step at $t = 10$ seconds shows the response due to an increase in the compressor input while keeping the stack current constant. The opposite scenario is shown at $t = 14$ seconds. The response between the 10th and 14th seconds shows that even though the stack voltage v_{st} and power P_{st} increase, the net power $P_{net} = P_{st} - P_{cm}$ actually decreases due to the increased parasitic loss (P_{cm}). The low-order model described here is compared through simulation with the fuel cell model that includes detailed anode model, manifold filling dynamics and membrane humidity [16, 18]. The comparison shows that the equations (2) - (21) capture the dynamics of voltage and starvation characteristics when humidity and temperature are well controlled.
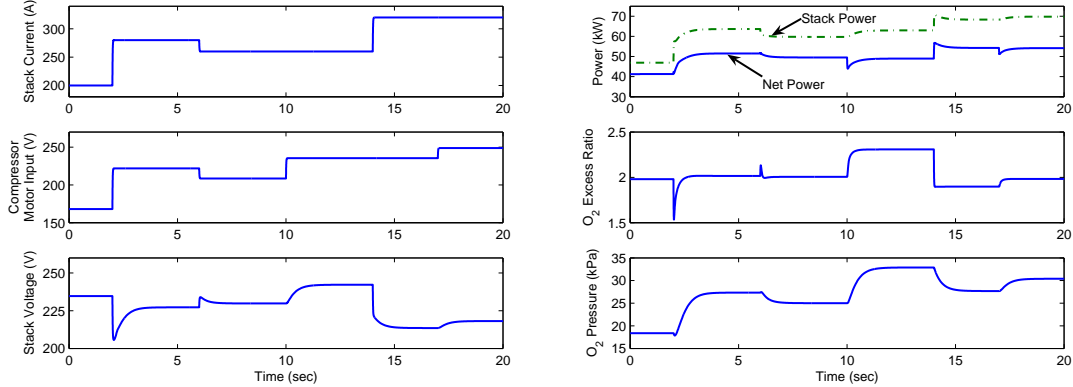
7

Figure 3: Simulation results of fuel cell reactants supply model

2.3 Control of air supply

The FC compressor is controlled to supply the air flow to the cathode that is necessary for the reaction associated with the current drawn I_{st} from the fuel cell as shown in Figure 4. For several reasons [2, 18] air supplied to the cathode should exceed the air necessary for reaction. The oxygen excess ratio λ_{O_2} in (13) is a convenient lumped variable, which if regulated to a desired value ($\lambda_{O_2}^{ref} = 2$) ensures adequate supply of oxygen in the cathode.

We consider here the case where the compressor is driven from the fuel cell. The total current drawn from the fuel cell stack, I_{st} is defined by the input current I_{in} which is the current from the FC to the DC-DC converter, and augmented by the current load drawn from the all of the auxiliaries and particularly compressor, I_{cm}

$$I_{st} = I_{in} + I_{cm}. \tag{22}$$

Here it is considered that the compressor motor contributes to the largest percent of losses through the current drawn I_{cm} directly from the stack bus. To calculate the current consumed by the compressor, we assume again that the compressor motor has an ideal power transformer and supplies the necessary power P_{cm} by drawing a current I_{cm} at the stack bus voltage v_{st}:

$$I_{cm} = \frac{P_{cm}}{v_{st}} \tag{23}$$

where v_{st} is given by the polarization curve in [16, 18]. Thus compressor current is implemented so that P_{cm} is simply drawn from the stack through a fast filter that emulates the motor control unit.

The control objective of regulating performance variable λ_{O_2} can be achieved by a combination of feedback and feedforward algorithms that automatically define the compressor motor voltage input v_{cm}. Since the oxygen excess ratio λ_{O_2} is not directly measured, we control λ_{O_2} indirectly by measuring the compressor flow W_{cp} and the demanded load I_{st}. Figure 4 shows the feedback and feedforward controllers which are designed to regulate the oxygen excess ratio.

Specifically, feedforward control to air compressor voltage v_{cm}^{ff} can be applied based on the stack current I_{st}, $v_{cm}^{ff} = f(I_{st})$. The function $f(I_{st})$ is determined by the balance of oxygen
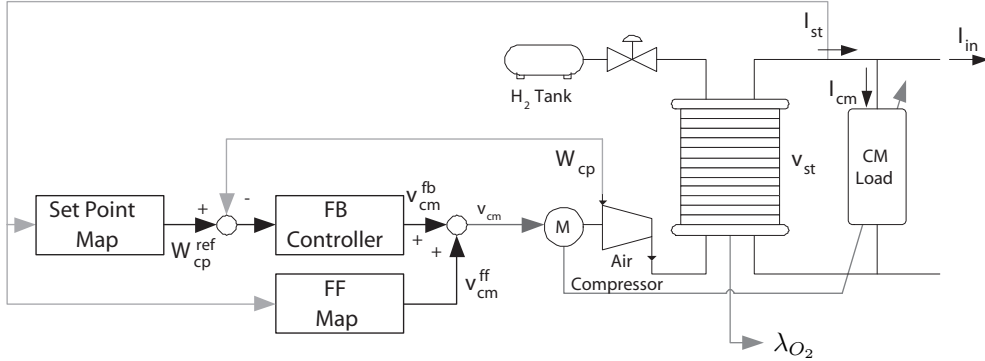
8

Figure 4: Schematic of fuel cell with air flow control using compressor

mass consumed for the stack current and the compressor map from v_{cm} to W_{cp}, thus it can be programmed or stored in a lookup table in a computer. The feedforward control can accurately regulate λ_{O_2} to its desired value at steady state if all the model parameters are known. Also adding a feedforward controller may be helpful for this problem because the compressor voltage can be scheduled immediately after the current demand is issued, avoiding sensor delays associated with any feedback compensation. To reduce potential errors associated with modeling errors or device aging, a feedback controller v_{cm}^{fb} can be combined with the feedforward controller based on the compressor flow measurement W_{cp}. The feedback controller ensures that the compressor flow reaches fast a desired value W_{cp}^{ref} that is calculated base on the stack current [17]. Namely a proportional and integral (PI) controller can be applied to the difference of W_{cp} and W_{cp}^{ref}. The voltage control command can be written as

$$
\begin{aligned}
v_{cm}(t) &= v_{cm}^{ff}(t) + v_{cm}^{fb}(t) \\
&= f(I_{st}) + K_P \left(W_{cp}^{ref}(I_{st}) - W_{cp}(t) \right) + K_I \int_0^t \left(W_{cp}^{ref}(\tau) - W_{cp}(\tau) \right) d\tau.
\end{aligned} \tag{24}
$$

Details of more complex controllers such as dynamic cancelation and observer-based feedback designs with various performances and robustness can be found in [17]. Note that the configuration in [17] implied that an auxiliary power unit supplies the compressor motor. The controller in equation (24) ensures there is adequate air flow supply to the stack, but allows the cathode pressure to drift as implied by equation (2), (3) and (5). Results on control of the air flow and the cathode pressure using a compressor and a back throttle can be found in [21].

Figure 5 shows the closed-loop performance for two different controller gains K_p. During a step input of net current I_{in}, the oxygen excess ratio initially drops because the additional air flow that can compensate the amount of increased current has not yet reached the cathode. The oxygen excess ratio λ_{O_2} recovers quickly due to the feedforward control and settles to the desired steady-state value with no error due to the PI controller. Higher controller gain shown in dashed line improves the W_{cp} tracking performance by employing larger control input signal v_{cm}. Despite the improvement in W_{cp}, the λ_{O_2} regulation degrades. The reason for this degradation is critical for the compressor controller tuning. First, the current drawn from the fuel cell by the compressor increased in the case of high gain PI controller. Second, the high gain controller decreases the W_{cp} overshoot which delays the delivery of the necessary air flow to the cathode (further downstream the compressor)

Thus, the difficulty and control limitations are more pronounced in the case where the compressor is powered directly by the fuel cell and not an auxiliary power unit. In fact the limitation
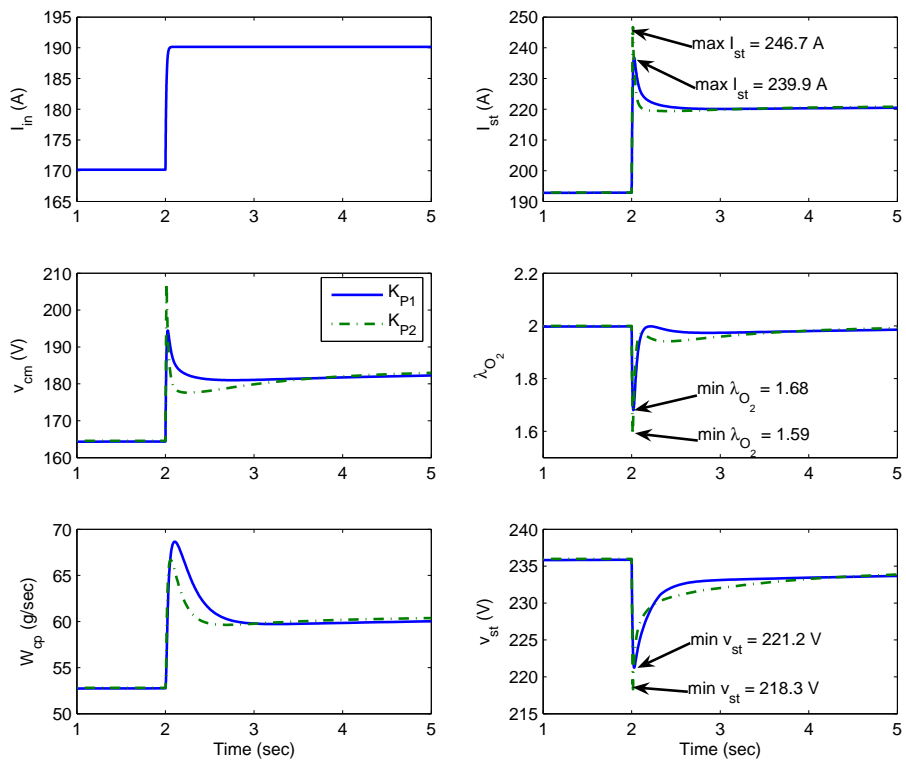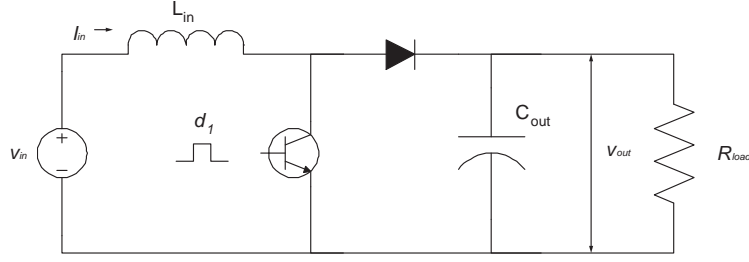
Figure 5: Fuel cell control simulation

Figure 6: DC-DC boost converter

in controlling oxygen starvation arises from the compressor and fuel cell electric coupling and not from the manifold filing dynamics as frequently quoted in literature [5, 17, 21, 22]. Indeed, when the compressor power is drawn directly from the fuel cell, there is a direct conflict between regulating the compressor air mass flow and regulating the oxygen excess ratio. Fast air flow control requires large compressor power that increases the current drawn from the stack. This direct coupling between the actuator signal v_{cm} and the performance variable λ_{O_2} especially at high frequencies exacerbates the difficulties in controlling the air flow to the fuel cell during step increase in load.

3 DC-DC converter

3.1 DC-DC converter model

The DC-DC converter transforms the DC fuel cell stack power to output voltage-current requirements of the external power devices that connect to a FC system. Here we consider a boost converter (shown in Figure 6) that can be used in PEM fuel cell applications. The input voltage v_{in} and input current I_{in} of the converter are the FC output voltage and the net FC current. In steady-state, the converter functionality can be described by

$$
\begin{aligned}
v_{in} I_{in} &= v_{out} I_{out}, \\
I_{in} d_1 &= I_{out}.
\end{aligned}
\tag{25}
$$

The output voltage v_{out} and current I_{out} depend on the duty ratio d_1 of the solid state switch in the circuit. The inductance of input inductor L_{in}, the capacitance of output capacitor C_{out} and the resistance of the load R_{load} are shown in Figure 6.

In this study, the boost converter is selected for 50 kW power and based on 400 V output voltage with nominal input voltage is 250 V and thus nominal input current is 200 A. Ideally the input power is processed in a converter with 100 % efficiency. Actual efficiency is slightly less than 100 % due to the losses in the inductor, capacitor, transformer, switch and controller circuit. A typical boost converter for PEM fuel cell application has about 95 % efficiency when the voltage boost ratio is approximately two [15].

Increasing L_{in} reduces the ripple of the input current. Although large L_{in} protects the stack from high frequency AC current, the associated increase in resistance might decrease the converter efficiency. The size of C_{out} is usually determined by the ripple specification of output voltage. Other considerations such as the voltage and current limit of the capacitor should also be accounted especially due to high voltage and current values associated with FC applications. For the subsequent dynamic analysis, the values of inductor and capacitor are selected to be as $L_{in} = 1$ mH and $C_{out} = 1200$ μF.

An average nonlinear dynamic model can be used to approximate the boost converter switching dynamics [13]:

$$L_{in}\frac{dI_{in}}{dt} = v_{in} - (1 - d_1)v_{out},$$
$$C_{out}\frac{dv_{out}}{dt} = (1 - d_1)I_{in} - \frac{v_{out}}{R_{load}}. \qquad (26)$$

The inputs to the converter, based on realistic FC operation, are the duty ratio d_1, the input voltage v_{in}, and the output current, $I_{out} = v_{out}/R_{load}$. Linearization and Laplace transformation from these inputs to the output voltage v_{out} provide the following transfer functions [6]:

$$v_{out}(s) = G_d(s)d_1(s) + G_v(s)v_{in}(s) - Z_{out}(s)I_{out} \qquad (27)$$

$$G_d(s) = \frac{\frac{v_{out,n}}{(1-d_{1,n})R_{load,n}C_{out}}\left[\frac{(1-d_{1,n})^2 R_{load,n}}{L_{in}} - s\right]}{s^2 + \frac{1}{R_{load,n}C_{out}}s + \frac{(1-d_{1,n})^2}{L_{in}C_{out}}}$$

$$G_v(s) = \frac{\frac{1-d_{1,n}}{L_{in}C_{out}}}{s^2 + \frac{1}{R_{load,n}C_{out}}s + \frac{(1-d_{1,n})^2}{L_{in}C_{out}}}$$

$$Z_{out}(s) = \frac{\frac{1}{C_{out}}s}{s^2 + \frac{1}{R_{load,n}C_{out}}s + \frac{(1-d_{1,n})^2}{L_{in}C_{out}}}$$

where $d_{1,n}$ is the nominal duty ratio and $R_{load,n}$ is the nominal load resistance. The transfer function Z_{out} is called converter impedance and represents the effect of small load (current) changes to v_{out}. Due to the zero at the origin of Z_{out} the steady-state output voltage is not affected by a step change in load. This capability to reject load disturbances (variation in I_{out}) and regulate the output voltage (v_{out}) is desirable. However, a zero at $s = 0$ corresponds to the derivative of the disturbance input causing large deviation in v_{out} during a step change in load. Thus, although the zero at the origin helps the steady-state performance, it deteriorates the transient performance. The impedance can also represent the dynamics of R_{load} to v_{out} when the electric load is purely resistive which is typical for automotive or backup power applications.

The output voltage dynamics depends on nominal power level and input voltage which are reflected in the the open-loop transfer function through different $d_{1,n}$ and $R_{load,n}$ values. It can be shown that the characteristic equation given by the denominator of the transfer function of the transfer functions in (27) has under-damped behavior for typical combinations of L_{in}, C_{out}, $d_{i,n}$ and $R_{load,n}$. The damping decreases when power increases or $R_{load,n}$ decreases in $\zeta = \frac{1}{2R_{load,n}(1-d_{1,n})}\sqrt{L_{in}/C_{out}}$. The gain and phase Bodes plot of the transfer function G_d in (27) shown in Figure 7 describes the open-loop dynamics (from control input d_1 to performance variable v_{out}).

Low damping causes undesirable output oscillations that can be reduced with judicious control design as discussed below. As the Bode plots indicate, the open loop converter has fast dynamics with natural frequency $\omega_n = (1 - d_{1,n})/\sqrt{L_{in}C_{out}}$ approximately at 1000 rad/sec. The fast converter dynamics cause abrupt changes in I_{in} and act as a disturbance to the fuel cell. Therefore, the converter control design has to reduce this high frequency disturbance to the fuel cell by providing damping, or in other words, filtering the current I_{in} drawn from the FC.

3.2 DC-DC converter control

The converter control objective is to maintain constant bus voltage despite variations in the load and the input (fuel cell) voltage. In the fuel cell application, the converter operates in large range
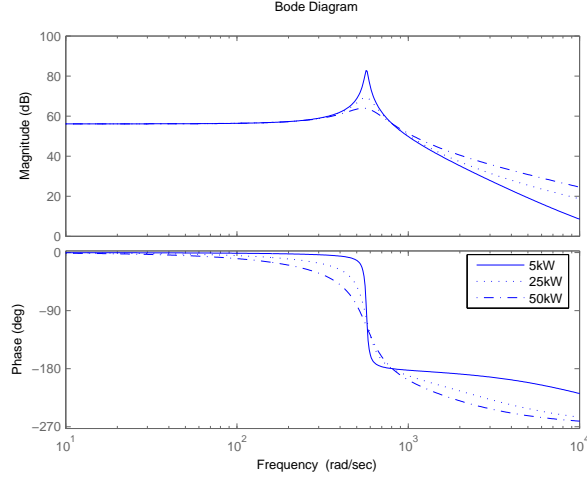
Figure 7: Open-loop dynamics of DC-DC converter transfer function G_d for different loads
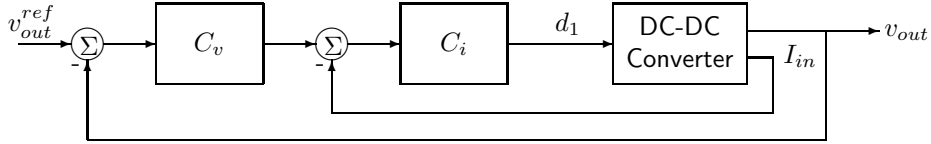

Figure 8: Sequential loop control

of power. We thus consider disturbances in $1/R_{load}$ that can capture the large load variation better than the output current I_{out} formulation in (27).

Nonlinear control techniques in [7] were employed to handle large variations in converter loads. We employ linear control techniques similar to [6] and formulate the bus voltage regulation problem using the control structure in [11]. A two-degrees of freedom (2DOF) controller shown in Figure 8 and presented in [13] is formulated.

In this control scheme, the outer loop controller C_v is composed of a PI controller for zero steady-state error. Then the output from C_v can be the virtual reference of I_{in} which becomes the current drawn from the fuel cell when the converter connects to the fuel cell. Nonlinear logics such as slew rate limiter, saturation or any kind of filter can be added to shape the current from the fuel cell stack [15]. Adding a proportional feedback C_i around the I_{in} measurement is equivalent to derivative controller which is needed to damp the typically undamped DC-DC converter dynamics as shown in section 3.1. Although C_i is designed as proportional controller, it acts as a derivative control for v_{out} because I_{in} is related to the derivative of v_{out} as shown in (26).

The controller can be written as

$$d_1(s) = -K_{Dv}I_{in}(s) - K_{Pv}v_{out}(s) - \frac{K_{Iv}}{s}v_{out}(s) \tag{28}$$

and formulated as state feedback when an integrator is add to the states. The optimal state feedback gains K_{Dv}, K_{Pv} and K_{Iv} can be selected from a linear quadratic regulator design [11].

13
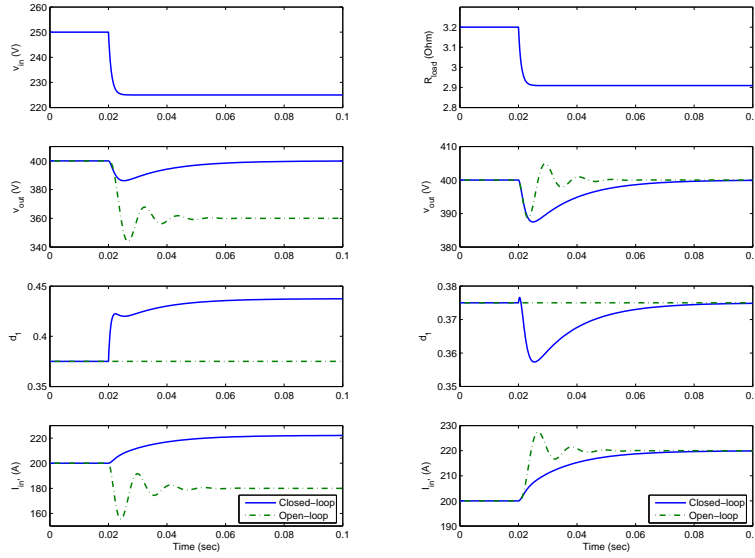
(a) input voltage change   (b) load resistance change

Figure 9: Simulation results of the DC-DC converter

With known gains two equivalent controllers, C_v and C_i are separated

$$C_v(s) = \frac{K_{Pv}}{K_{Dv}} + \frac{K_{Iv}}{K_{Dv}s}$$
$$C_i(s) = K_{Dv} \tag{29}$$

to allow nonlinear current limiters to be inserted for the virtual reference command input to I_{in}.

Figure 9 shows simulations results of the boost converter with two degree of freedom controllers (solid line) and the open-loop performance (dashed line). First, a step decrease of input voltage from 250 V to 225 V is applied to emulate fuel cell voltage which corresponds to 70 mV average cell voltage drop. During this change, shown in (a), the duty ratio d_1 increases and draws more current from the input source. The performance variable v_{out} recovers within 0.1 second. The controller can be tuned to handle the input voltage change faster at the expense of faster transient in current drawn from the fuel cell I_{in}. The graphs in column (b) show the closed-loop response during a load change. The load change corresponds to increase in power from 50 kW to 55 kW. In this situation, steady-state voltage regulation is not a problem because the DC gain of the impedance transfer function Z_{out} is zero as discussed in Section 3.1. Nevertheless, the controller we design reduces d_1 for a short time. This decrease helps filter the sharp and oscillatory current in I_{in} that would have occurred otherwise (shown in dashed line). Here it can be observed that the closed-loop I_{in} increases and settles to the next steady state level in both input voltage change and output power change. This behavior clarifies the causality between the fuel cell and converter dynamics, where the fuel cell becomes a current source in the output voltage regulation problem.

14
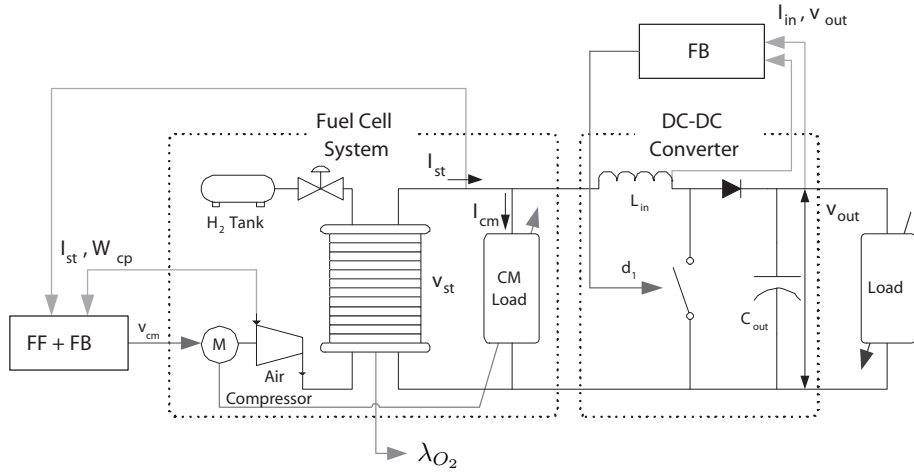
(a) Decentralized control scheme
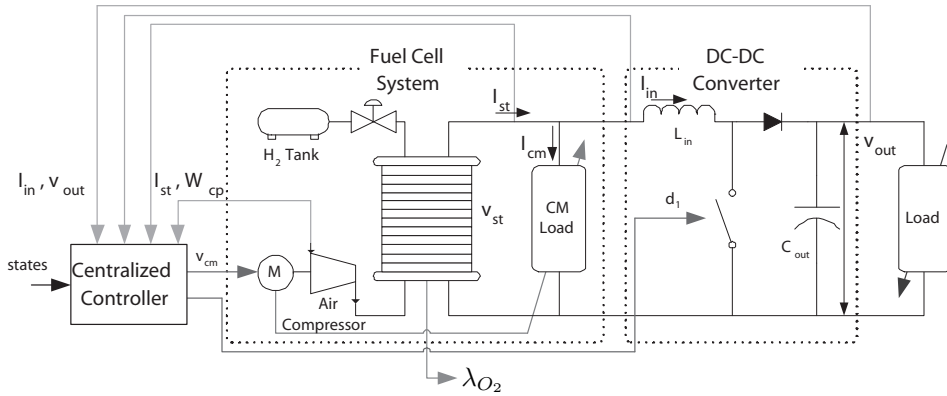
(b) Coordinated control scheme

Figure 10: Control schemes for fuel cell power system

4 Connecting the converter with the fuel cell

The fuel cell, with the controlled compressor, is connected with the controlled converter to form an autonomous power supply. In an industrial application, the fuel cell with its compressor and compressor controller is viewed as one component and the converter with its controller as another as shown if Figure 10 (a). Typically, these two components are provided by different manufacturers based on some initial specifications. The two controllers are calibrated separately and small corrections are performed after the two components are connected. This control architecture is called decentralized, and the calibration is called sequential, because one controller is tuned and then the other is re-tuned to minimize interactions between the two components. The process is sometimes tedious and can be suboptimal even after many iterations.

Another calibration that chooses the right calibration by taking into account the component interaction is called multivariable and results in a centralized controller as shown in Figure 10 (b). The centralized controller, indeed, achieves better performance than the decentralized even after several iterations. Decentralized control is successful if there is minimal coupling between the two systems. In our case, the performance variables λ_{O_2} and v_{out} are conflicting with each other and
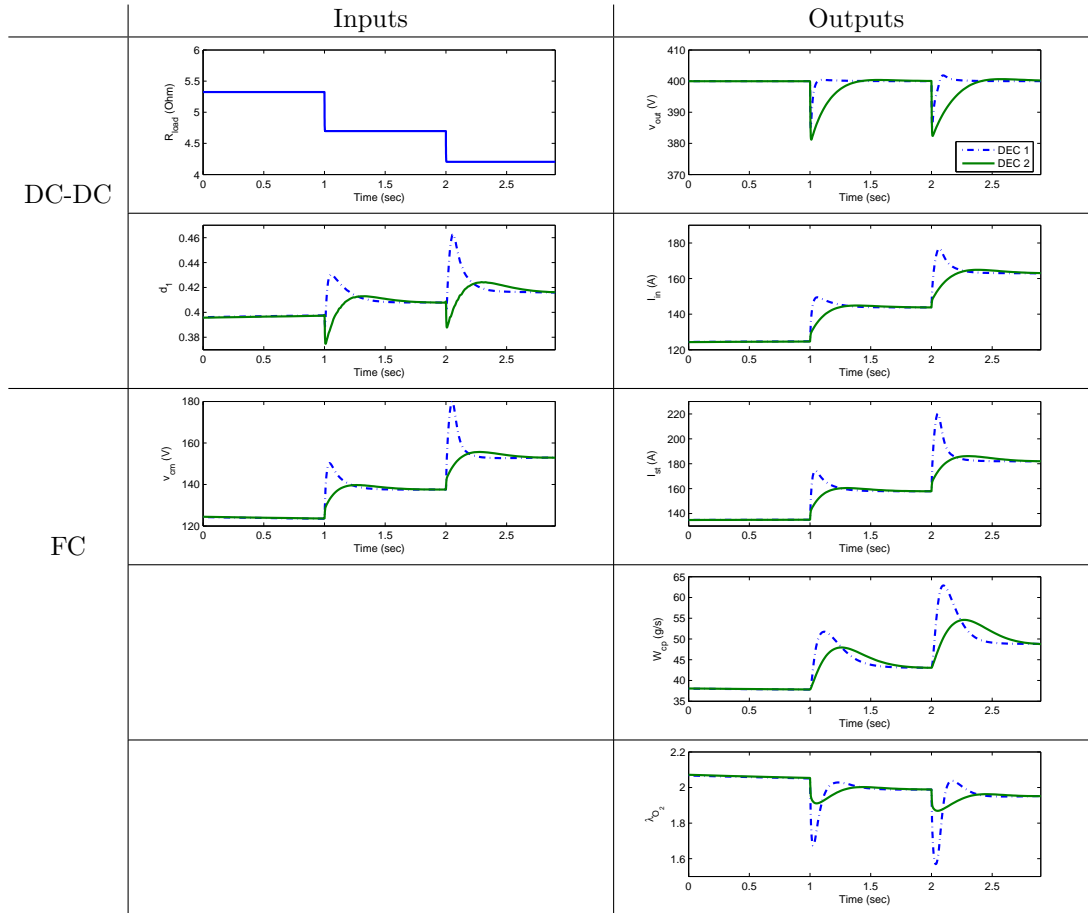
15

Figure 11: Simulation results of fuel cell power system: decentralized control

result in a challenging calibration problem.

Figure 11 shows the simulation results of the fuel cell power system with two decentralized controllers in a series of step load resistance changes. As can be seen in dashed line, when the converter controller acts fast to regulate v_{out}, there is large excursion in λ_{O_2}. Specifically, the duty ratio d_1 increases instantaneously after the step load change in R_{load} in order to regulate v_{out}. This increase in d_1 causes a sudden input current I_{in}, which causes unacceptable λ_{O_2} excursion. The effect of load increase becomes severe due to the compressor current drawn from the FC, which can be estimated by observing the compressor input v_{cm}, the stack current I_{st}, and the net current I_{in}. Detuning of the converter controller is necessary to avoid this fast interaction with the fuel cell. The solid line shows the simulation results after the detuning. Now the duty ratio initially decreases even if the the load increases filtering the FC current and avoiding the large λ_{O_2} excursion. For these converter gains, the output voltage recovers slowly demonstrating the severe tradeoff associated with the decentralized architecture controller.

As we have seen in the previous section, the two performance outputs are conflicting. It is, thus, not clear if any control design can improve the performance of both outputs. A centralized, model-based controller is designed to define the optimal signals within the conflict. The approach is known as linear quadratic regulator(LQR). We employ linearization of the state-space repre-

16

sentation in Section 2 and 3 with states $x = (p_{O_2}, p_{N_2}, \omega_{cp}, p_{sm}, I_{in}, v_{out})$ and state equations of the integrators

$$\frac{d}{dt} \begin{bmatrix} q_1 \\ q_2 \end{bmatrix} = \begin{bmatrix} W_{cp}^{ref} - W_{cp} \\ v_{out} \end{bmatrix} \tag{30}$$

at 40 kW power level. The optimal control law uses a state feedback with integral control

$$\begin{bmatrix} v_{cm} \\ d_1 \end{bmatrix} = K_{LQR} \begin{bmatrix} p_{O_2} \\ \vdots \\ v_{out} \end{bmatrix} + K_{I,LQR} \begin{bmatrix} q_1 \\ q_2 \end{bmatrix} \tag{31}$$

The sixteen unknowns elements of the controller gain K_{LQR} and $K_{I,LQR}$ are derived based on the minimization of a quadratic cost function

$$Q = \int_0^\infty \left(l_1 \lambda_{O_2}^2(t) + l_2 v_{out}^2(t) + l_3 q_1^2(t) + l_4 q_2^2(t) + r_1 v_{cm}^2(t) + r_2 d_1^2(t) \right) dt. \tag{32}$$

that explicitly depends on the performance variables λ_{O_2} and v_{out} through the weights l_1 to l_4. The actuator cost is added to the cost function through the weight r_1 and r_2 to prevent excessive actuator inputs, which is especially useful for the air compressor controller. Different coefficients q and r can be applied in Q for tuning the optimal control law (31).

The linear simulations of the coordinated controllers with two different cost functions are shown in Figure 12. The detuned decentralized controller (DEC2) is also shown with dash-dot line for comparison. A step resistance change input is applied intending to increase output power from 40 kW to 50 kW. The centralized controller CEN1 in dashed line is designed to match the v_{out} recovery of the detuned, decentralized controller DEC2, but performs considerably better than the decentralized controller in regulating λ_{O_2}. The relatively slow recovery of λ_{O_2} from all controllers is due to low v_{cm} controller gain which is already discussed in the FC controller design. The solid line shows that the coordinated controller has the capability to improve both performance outputs at the same time using the optimal design. The output voltage v_{out} recovers three times faster than the decentralized case without significant degradation of λ_{O_2}. Specifically, the voltage recovery of the centralized controller CEN1 ensures 10 kW power increase in 0.1 seconds whereas the best decentralized controller we could design allows the same 10 kW power increase in 0.3 seconds. The control strategy can be observed with the response in the solid line. The duty ratio initially drops to protect the FC while waiting for the air supply to increase. When the compressor ramps up then d_1 increases rapidly to recover the output voltage v_{out}. These benefits on both performances occur mostly from the communication and coordination in the system.

The drawback of the coordinated control is the increase of computation for measurement and state estimation. The estimation problem and computation requirements will be explored in future work. The centralized controller is tuned based on the full model of the (combined) fuel cell, compressor, and converter. Obtaining a model similar to the one we presented might be an unrealistic expectation due to proprietary reasons in such highly-engineered devices. Thus, the centralized controller designed here serves as a way of defining the requirements for the minimal communication between the fuel cell controller and the converter controller.

5   Conclusion

Modeling and analysis of a load following FC combining a fuel cell system and a DC-DC converter is shown in this paper. A low-order FC system model has been developed using physical principles and stack polarization. The inertial dynamics of the compressor, manifold filling dynamics and
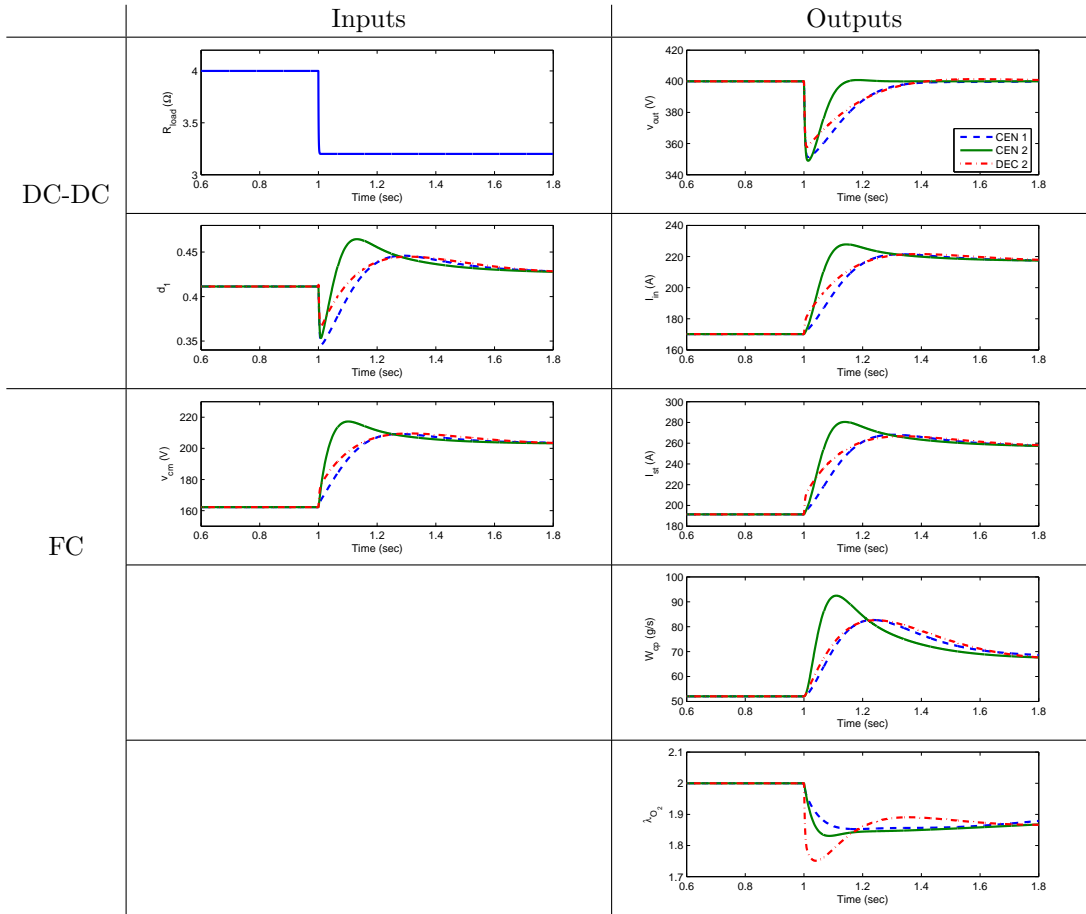
Figure 12: Simulation results of fuel cell power system: centralized control

partial pressures are captured. An average continuous in time modeling approach that approximates the converter switching dynamics is applied. The direct conflict between the air supply in FC and the voltage regulation in the converter is elucidated.

Then a model-based controller is designed to regulate both the FC oxygen excess ratio and the bus voltage using decentralized and coordinated control architectures. A severe limitation arises when no hybridization dictates that the air supply compressor is powered directly from the FC. We show that coordination between the compressor and the converter controllers can alleviate the tradeoff between the two performances.

Our comparison was performed at an operating range for medium to high loads. The performance and calibration requirements of the two controller architectures for wide operating range of power will be investigated in future work. So far we have verified that the linear decentralized controller achieves good performance for wide range of power (20 - 60 kW net power). We need to perform similar comparison after we design and integrate an observer for the estimation of all the states for the centralized controller.

We have not tested the controllers during shut-down or start-up conditions, primarily due to lack of a validated model at these operating points. A bench top experiment will be used for testing all these results. This study can also be extended to the design and optimization of FC hybrid power system without neglecting the dynamic interactions among power sources.

Acknowledgements

Nomenclature

$\bar{R}$ Universal gas constant (= 8.3145 J/(mol·K))

A Active area (cm^2)

C Capacitance (F)

C_p Specific heat capacity of the air (= 1004 J/(mol·K))

d Duty ratio

F Faraday number (= 96,485)

I Current (A)

i Current density (A/cm^2)

J Inertia (kg·m^2)

K Controller gain

k Flow constant (kg/(s·Pa)), Motor constant (V/(rad/sec), N-m/A)

L Inductance (H)

M Molar mass (kg/mol)

n	Number of cells
p	Pressure (Pa)
Q	Cost function
R	Resistance (Ω)
T	Temperature (K)
V	Volume (m^3)
v	Voltage (V)
W	Mass flow rate
w	Humidity ratio
x	Mass fraction, State
y	Molar ratio

Greek letters

η	Efficiency
γ	Ratio of the specific heat capacities of the air ($= 1.4$)
λ_m	Membrane water activity
λ_{O_2}	Oxygen excess ratio
ω	Rotational speed (rad/sec)
ϕ	Relative humidity

Subscripts

an	Anode
atm	Atmospheric
ca	Cathode
cm	Compressor motor
cp	Compressor
D	Derivative
fc	Fuel cell
H_2	Hydrogen
I	Integrator
in	Input
$load$	Load

LQR	linear quadratic regulator
max	Maximum
n	Nominal
N_2	Nitrogen
O_2	Oxygen
out	Output
P	Proportional
rct	Reacted
sat	Saturation
sm	Supply manifold
st	Stack
v	Vapor, Voltage

Superscripts

fb	Feedforward
ff	Feedback
ref	Reference

References

[1] Amphlett JC, Mann RF, Peppley BA, Roberge PR, Rodrigues A. 1996. A model predicting transient responses of proton exchange membrane fuel cells. *Journal of Power Sources.* **61**: 183-188.

[2] Boehm G, Wilkinson DP, Khight S, Schamm R, Fletcher NJ. 2002. Method and appratus for operating a fuel cell. *United States Patents 6,461,741.*

[3] Cunningham JM, Moore R, Ramaswamy S, Hauer K. 2003. A comparison of energy use for a direct-hydrogen hybrid versus a direct-hydrogen load-following fuel cell vehicle. *SAE Papers 2003-01-0416.*

[4] Cunningham JM, Hoffman MA. 2001. A Comparison of high-pressure and low-pressure operation of PEM fuel cell systems. *SAE Papers 2001-01-0538.*

[5] Cunningham JM, Hoffman MA, Moore RM, Fredman DJ. 1999. Requirements for a flexible and realistic air supply model for incorporation into a fuel cell vehicle system simulation. *SAE Papers 1999-01-2912.*

[6] Erickson RW, Maksimovic D. 2001. *Fundamentals of Power Electronics.* 2nd ed. Kluwer.

[7] Escobar G, Ortega R, Sira-Ramírez H, Vilain J, Zein I. 1999. An experimental comparison of several nonlinear controllers for power converters. *IEEE Control System Magazine.* **19**(1): 66-82.

[8] Friedman DJ. 1999. Maximazing Direct-Hydrogen PEM Fuel Cell Vehicle Efficiency - Is Hybridization Necessary?. *SAE Paper 1999-01-0530.*

[9] Fronk MH, Wetter DJ, Masten DA, Bosco A. 2000. PEM fuel cell system solutions for transportation. *SAE Paper 2000-01-0373.*

[10] Gelfi S, Stefanopoulou AG, Pukrushpan JT, Peng H. 2003. Dynamics of lower-pressure and high-pressure fuel cell air supply systems. *Proceedings of the 2003 American Control Conference.* **3**: 2049-2054.

[11] Gezgin C, Heck BS, Bass RM. 1997. Control structure optimization of a boost converter: An LQR approach. *28th Annual IEEE Power Electronics Specialists Conference.* **2**: 901-907.

[12] Ishikawa T, Hamaguchi S, Shimizu T, Yano T, Sasaki S, Kato K, Ando M, Yoshida H. 2004. Development of next generation fuel-cell hybrid system - consideration of high voltage system. *SAE Papers 2004-01-1304.*

[13] Krein PT. 1998. *Elements of Power Electronics.* Oxford: New York.

[14] Larminie J, Dicks A. 2003. *Fuel Cell Systems Explained.* 2nd Ed. John Wiley & Sons.

[15] National Energy Technology Laboratory. 2004. *Fuel Cell Handbook.* 7th ed.

[16] Pukrushpan JT, Peng H, and Stefanopoulou AG. 2004. Control-oriented modeling and analysis for automotive fuel cell systems. *ASME Journal of Dynamic Systems, Measurement, and Control.* **126**(1): 14-25.

[17] Pukrushpan JT, Stefanopoulou AG, Peng H. 2004. Control of fuel cell breathing. *IEEE Control System Magazine.* **24**(2): 30-46.

[18] Pukrushpan JT, Stefanopoulou AG, Peng H. 2004. *Control of fuel cell power systems: Principles, modeling, anylysis and feedback design.* Springer.

[19] Rajashekara K. 2000. Propulsion system strategies for fuel cell vehicles. *SAE Paper 2000-01-0369.*

[20] Ramaswamy S, Moore R, Cunningham JM, Hauer KH. 2004. A comparison of energy use for a indirect-hydrocarbon hybrid versus an indirect-hydrocarbon, load-following fuel cell vehicle. *SAE Papers 2004-01-1476.*

[21] Rodatz P, Paganelli G, Guzzella L. 2003. Optimizing air supply control of a PEM fuel cell system. *Proceedings of the 2003 American Control Conference.* **3**: 2043-2048.

[22] Sun J, Kolmanovsky I. 2004. Load governor for fuel cell oxygen starvation protection: A robust nonlinear reference governor approach. *Proceedings of the 2004 American Control Conference.* 828-833.

[23] Thomas P. 1999. *Simulation of Industrial Processes for Control Engineer.* Butterworth Heinemann. London.

[24] Wang Y, Wang C. 2005. Transient analysis of polymer electrolyte fuel cells. *Electrochimica Acta.* **50**(6): 1307-1315.

[25] Yang W, Bates B, Fletcher N, Pow R. 1998. Control challenges and methodologies in fuel cell vehicle development. *SAE Papers 98C054.*